

Mobile Topological Su-Schrieffer-Heeger Soliton in a Josephson Metamaterial

Dushko Kuzmanovski,¹ Rubén Seoane Souto,² Patrick J. Wong,^{1,3} and Alexander V. Balatsky^{1,3}

¹*Nordita, KTH Royal Institute of Technology and Stockholm University Hannes Alfvéns väg 12, SE-106 91 Stockholm, Sweden*

²*Instituto de Ciencia de Materiales de Madrid (ICMM),*

Consejo Superior de Investigaciones Científicas (CSIC),

Sor Juana Inés de la Cruz 3, 28049 Madrid, Spain

³*Department of Physics, University of Connecticut, Storrs, Connecticut 06269, USA*

(Dated: December 7, 2023)

Circuits involving arrays of Josephson junctions have emerged as a new platform for exploring and simulating complex bosonic systems. Motivated by this advance, we develop and theoretically analyze a one-dimensional bosonic system with sublattice symmetry, a bosonic Su-Schrieffer-Heeger model. The system features electrostatically controlled topological mid-gap states that we call soliton states. These modes can be measured using either spectroscopy through a normal lead or admittance measurements. We develop a protocol to adiabatically shuttle the position of these topological soliton states using local electrostatic gates. We demonstrate a nearly perfect fidelity of soliton shuttling for timescales within experimental reach.

I. INTRODUCTION

A recent paradigm in quantum technology is the advent of quantum computation. The hardware of a general-purpose quantum computer which has the ability to generically run any quantum algorithm [1] has not yet been realized. A complementary approach is utilizing special purpose-built hardware [2] for simulating specific many-body Hamiltonians. Platforms based on ion traps [3], cold atoms [4], and circuits involving Josephson junctions [5] have been used for this purpose. Superconducting platforms show advantages regarding scalability, low power consumption, low noise, and ease of interfacing. These systems involve several islands that can exchange Cooper pairs via tunneling. Fabrication advances have enabled islands to be defined with sub-micron precision, allowing the investigation of superconductor-insulator transition [6–9], including anomalous metal phases [10]. Apart from the current interest in quantum information processing applications, quantum metamaterials based on Josephson junction arrays offer the possibility of creating platforms for investigating the effects of circuit quantum electrodynamics [11–13].

In this work, we theoretically analyze the formation of topological states in a chain of superconducting (SC) islands connected via Josephson junctions forming a Josephson junction array (JJA), Fig 1a. We work in a regime where junction shunt capacitances are negligible relative to gate capacitances. We consider that the Josephson energy between the islands has an amplitude that alternates, realizing a superconducting version of the Su-Schrieffer-Heeger (SSH) model. We demonstrate that local electrostatic gates can tune the position of these states, which can be detected by either tunneling or noise spectroscopy. For instance, detuning the energy of one island away from zero, which can be seen as adding a defect into the system, creates a topological state.

The SSH model is a paradigmatic topological insulator in one dimension [14–16]. It is characterized as a tight-

binding chain of 2-site unit-cell dimers with an intracell hopping t_1 and an intercell hopping t_2 . For a given termination of the chain, the model is either in a trivial insulator phase with a gapped spectrum, or in a topological phase with zero-energy states localized on its boundaries, depending on the ratio of the hopping elements, $t_2/t_1 < 1$ or $t_2/t_1 > 1$. The SSH model hosts localized states near domain walls, where the parity of the dimerization changes [16]. These localized in-gap states correspond to soliton states in the continuum theory of the SSH model [17] and we adopt this nomenclature in our discussion.

The bosonic SSH model has been realized in many other systems, such as optical waveguides [18], acoustic phonons [19], magnons [20–22], Rydberg atoms [23, 24], ultracold atoms [25–27], and superconducting transmons [28–30]. Furthermore, a similar concept to ours was considered where the elementary excitations were fluxons [31].

We develop a protocol to shuttle topological states along the chain by tuning the energy of adjacent islands. Topological states have orthogonal wavefunctions. Therefore, detuning additional sites would result in an exact crossing of the wavefunctions and a failure of the protocol. Instead, bringing the energy of the impurity island close to resonance, makes the ground state hybridize with the continuum. If the process is done adiabatically, there is no weight transferred to the continuum of states. In this way, there is a finite overlap of the wavefunction with the one where the soliton state is located at another position. The fast and efficient manipulation of soliton defect states can be utilized for implementing robust mesoscopic qubits, as well as racetrack-type quantum memories. [32–35]

The rest of this paper is organized as follows: In Sec. II we introduce the Hamiltonian governing a general JJA circuit and describe the parameter regime in which we obtain an effective tight-binding model. In Sec. III, we focus on a linear SSH chain with applied on-site potential as control of a soliton state. The main conclusions are

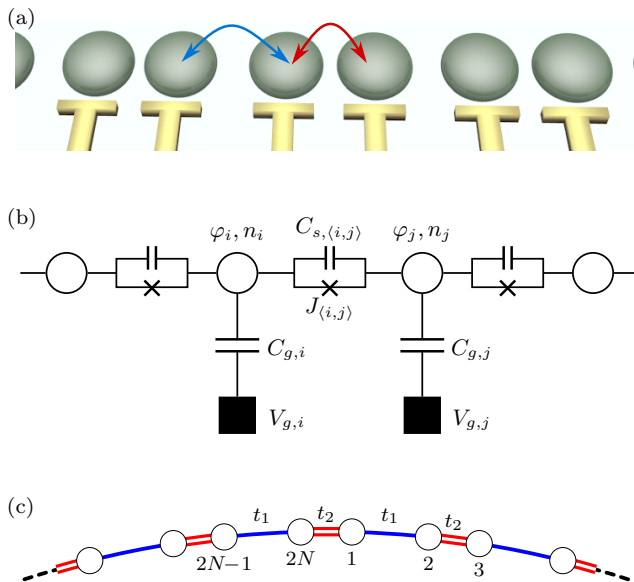


Figure 1. Three representative schematics of our Josephson junction array (JJA). (a) Representation of the chain of superconducting (SC) islands and voltage gates. Tunneling of Cooper pairs between nearby islands have alternating strengths symbolized by the blue and red arrows. (b) Circuit diagram of SC islands parameterized by φ and n coupled via JJs with critical currents $J_{(i,j)}$ and shunt capacitances $C_{s,(i,j)}$. Each island is capacitively coupled via a gate capacitance $C_{g,i}$ to an externally voltage-controlled gate $V_{g,i}$. (c) Effective SSH tight-binding model of a JJA in ring geometry with N dimers. The blue links are “weak” hopping amplitudes t_1 , while the red double links are “strong” hoppings t_2 . On-site potentials can be applied at each particular site.

given in Sec. IV. Additionally, we demonstrate an alternative shuttling protocol with low fidelity in Appendix A, and an animation of the two shuttling protocols over a whole ring in Appendix B.

II. MODEL

We model the physical realization of an array of Josephson junctions, Fig 1a by considering the circuit depicted in Fig. 1b. We write down a circuit Hamiltonian following the circuit theory of Refs. [36, 37] as

$$H_{\text{JJA}} = \frac{1}{2} \sum_{i,j} \tilde{C}_{i,j}^{-1} (n_i - n_{g,i}) (n_j - n_{g,j}) - \sum_{\langle i,j \rangle} J_{(i,j)} \cos(\varphi_i - \varphi_j), \quad (1)$$

where the mutual capacitance matrix is

$$\tilde{C}_{i,j} = \left(C_{g,i} + \sum_k C_{s,(i,k)} \right) \delta_{i,j} - C_{s,(i,j)}, \quad (2)$$

while the charge offsets $n_{g,i}$ due to applied gate voltages $V_{g,i}$ are

$$n_{g,i} = -C_{g,i} V_{g,i}. \quad (3)$$

The gate voltages are in principle time-dependent and serve to control the charge offset of every SC island. We have adopted a system of units in which $\hbar = 2e = 1$. In this case, the Josephson critical current and Josephson energy have the same units, and the inverse capacitance matrix equals the charging energy. The canonical commutation relation of the conjugate variables is

$$[\varphi_i, n_j] = i \delta_{i,j}, \quad (4)$$

with all the other commutators being identically zero. One can go over from phase and number variables to canonical bosonic creation-annihilation operators

$$b_i^\dagger = n_i^{\frac{1}{2}} e^{i\varphi_i}. \quad (5)$$

With this in mind, the Josephson term in Eq. (1) is reminiscent of a Cooper-pair hopping term, but includes interactions due to the non-linearity in Eq. (5). At the same time, the charging energy term in Eq. (1) is a four-point interaction term in terms of the creation/annihilation operators. We can approximate the Hamiltonian to a non-interacting one in the limit where charging energy dominates, so the number of Cooper pairs can only fluctuate between n_i and $n_i + 1$ (n_i being an integer) [38]. In this way, we arrive at the following non-interacting Cooper-pair hopping tight-binding Hamiltonian

$$\mathcal{H}_{\text{CPH}} = - \sum_{i,j} t_{i,j} b_i^\dagger b_j + \sum_i V_i n_i, \quad (6)$$

where the effective hopping element is

$$t_{i,j} = \frac{J_{(i,j)}}{2\sqrt{\langle n_i \rangle \langle n_j \rangle}}, \quad (7)$$

and the effective on-site potential is

$$V_i = \sum_j \tilde{C}_{i,j}^{-1} (\langle n_j \rangle - n_{g,j}). \quad (8)$$

The excitations of Eq. (6) are described by linear combinations of the on-site creation operators

$$\Gamma_\alpha^\dagger = \sum_i u_i^{(\alpha)} b_i^\dagger, \quad (9)$$

where the effective single-particle wavefunctions $u_i^{(\alpha)}$ of the α -th excitation satisfy the eigenvalue problem

$$- \sum_j t_{i,j} u_j^{(\alpha)} + V_i u_i^{(\alpha)} = \varepsilon_\alpha u_i^{(\alpha)}. \quad (10)$$

and the normalization condition

$$\sum_i |u_i^{(\alpha)}|^2 = 1. \quad (11)$$

Then, each of these modes is occupied according to a Bose-Einstein distribution

$$\langle \Gamma_\alpha^\dagger \Gamma_\beta \rangle = n_B(\varepsilon_\alpha/T) \delta_{\alpha,\beta}. \quad (12)$$

where $n_B(x) = 1/(\exp(x) - 1)$, and T is an effective temperature of the Cooper-pair subsystem. This is achieved by tuning a uniform shift of each V_i in Eq. (8) by a sufficiently large positive value, which, accordingly, shifts each excitation energy ε_α , so that the total number of Cooper pairs in the JJA, N_{CP} , satisfies

$$\langle N_{CP} \rangle = \sum_\alpha n_B(\varepsilon_\alpha/T). \quad (13)$$

The site occupancy that enters in Eqs. (7), (8) is given by

$$\langle n_i \rangle = \sum_\alpha \left| u_i^{(\alpha)} \right|^2 n_B(\varepsilon_\alpha/T). \quad (14)$$

III. RESULTS

The discussion in Sec. II is general and applies for any JJAs where charging energy dominates. We now focus on simulating the SSH model. To avoid finite-size effects, we consider a ring geometry with alternating hopping elements as indicated in Fig. 1c. In Sec. III A, we demonstrate how to introduce topological defects via applying on-site control potential. In Sec. III B, we give several descriptions of the topological nature of these soliton states bound to the control sites. Sec. III C gives a concrete experimentally measurable signature of the soliton state, and in Sec. III D we discuss a protocol for shuttling this soliton state to the neighboring dimer.

A. Electrostatically controlled soliton states

Here, we explore the topological states appearing in the system when creating a defect using on-site potential. This has the advantage that the position of the defect state is controllable with external voltages, whose time scales are, in principle, much faster than any electrostatic manipulation of the critical current in the JJ links.

We begin by discussing the effects of detuning one island (or an odd number of consecutive islands) away from resonance. For a sufficiently large detuning of the island, there is always an in-gap bound state, regardless of the ratio of bond hopping elements t_2/t_1 , as depicted in Fig. 2(a). The only difference is the direction towards which the wavefunction of such a state spreads: the soliton extends toward the direction of the strong broken bond. As the ratio between the hopping changes from $t_2/t_1 < 1$ to $t_2/t_1 > 1$, the position of the nearest-neighbor bond to the impurity site with larger hopping changes from right to left, and, with it, the orientation of the wavefunction spread, as shown on Fig. 2(b) for two

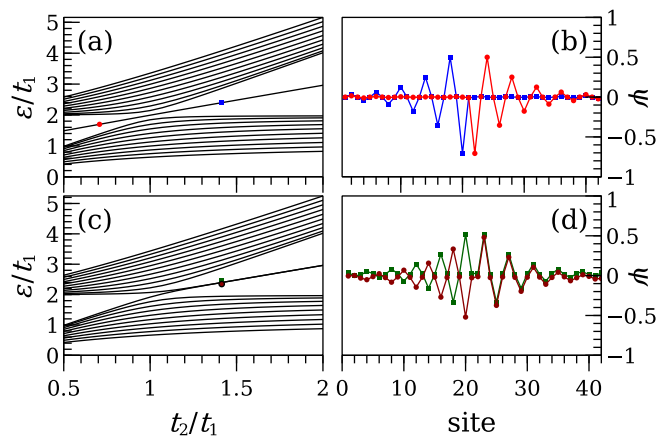


Figure 2. Spectrum (panels (a) and (c)) on a ring with $N = 21$ dimers as a function of the ratio of hopping terms t_2/t_1 . Panels (b) and (d) show the in-gap bound state real wavefunctions for the corresponding value of the parameter highlighted by dots in the left panels. The chemical potential is adjusted so that the average occupancy per site is $\langle n \rangle = 5.0$, and the effective temperature is always $T/t_1 = 0.0005$ for large on-site potential turned on at site 21 (panels (a) and (b)), and turned on at sites 21 and 22 (panels (c) and (d)).

representative values of the hopping-elements ratio. The behavior of the soliton wavefunction suggests that turning on a potential on another site would have the most significant detrimental effect due to destructive interference if it is on a neighboring site connected via a strong bond to the first potential site. Conversely, if connected via a weak bond, it would not hinder the spread of the SSH soliton wavefunction.

We now consider the effect of turning on a strong repulsive on-site potential on a dimer. Applying such a control potential profile has the same effect as removing a dimer (control dimer) and creating two artificial edges on the sites closest to the control dimer in the ring geometry. If the control dimer is linked to the rest of the chain via strong bonds, topological SSH states appear at the two sides of the of the dimer. No states appear in the case this links are weak.

Figure 2(c) shows the energy spectrum as a function of t_2/t_1 for a ring with detuned dimer that connects via t_2 (and connected via t_1 to the rest of the ring). When the ratio goes from less to above one, two topological states detach from the continuum and pin at the center of the gap. The wavefunctions of these two nearly-degenerate states are depicted in Fig. 2(d).

Since the soliton state of an SSH model is localized at a domain wall, the soliton can move by shifting the domain wall. Conventionally, this is accomplished by modulating the hopping parameters. However, instead of modifying the ratio t_2/t_1 , we can achieve an effective interchange of t_1 and t_2 by simply shifting the two positions of the on-site potentials by one site. We illustrate this possibility in the two panels in Fig. 3. In Fig. 3(a), dimer bond is strong, thus two mid-gap solitons, and in Fig. 3(b) the

bond is weak, and no mid-gap states are present.

B. Topological properties of the soliton state

In this subsection we wish to establish quantitatively the topological nature of the soliton states produced by introducing a potential on the control dimer. The localized wave function of band α takes the asymptotic form of $|u_{2j}^{(\alpha)}|^2 = |u_{j_0}^{(\alpha)}|^2 e^{-2j/\xi^{(\alpha)}}$ for site $2j$ in the limit of large system size where j_0 is the site hosting the localized soliton state and ξ is a localization length. We take the $2j$ -th site as the localized wave functions only have support on one sublattice. The localization length of the SSH model is $\xi_{\text{SSH}} = \ln(t_2/t_1)$ [16] where in the topological phase $t_2/t_1 > 1$. For the parameters chosen here ($t_2 = 2t_1$), $\xi_{\text{SSH}} = \ln(2) = 0.6931\dots$. For the wave function on the JJA ring with $V/t_1 = 100.0$ on the control dimer, we find that $\xi_{\text{JJA}}^{(20)} = 0.6925(1)$ and $\xi_{\text{JJA}}^{(21)} = 0.6932(1)$, in close agreement with the topological SSH value. The exact SSH value is valid for states with exactly zero energy, which is obtained in the limit of $V/t_1 \rightarrow \infty$, and where the wave function has support on one sublattice only, which is valid in the case of $N \rightarrow \infty$. We find that $|\xi_{\text{JJA}} - \xi_{\text{SSH}}| \sim 1/V$. This reinforces our identification of the localized state as being topological in origin.

For a one-dimensional system, its topology can be characterized by the winding number, or Zak phase [39]. A winding number can be calculated in the conventional way by taking the entire ring geometry to be representative of a periodic unit-cell and then proceeding to construct a momentum space representation. This is conventionally performed for the standard 2-sites per unit cell SSH model, however it has also been performed for the 4-site per unit cell SSH₄ model [40, 41], as well as arbitrarily large unit cell extensions of the SSH model [42]. The Zak phase of a band n is defined as

$$\gamma_n = \frac{1}{\pi} \int_0^{2\pi} dk A_n(k), \quad (15)$$

where $A_n(k) = i\psi_n^\dagger(k)\partial_k\psi_n(k)$ is the Berry potential of the n -th band with $\psi_n(k)$ the eigenvector for the n -th band of the momentum space Hamiltonian in the chiral basis. In the chiral basis the Hamiltonian takes the form of

$$H(k) = \begin{pmatrix} \epsilon & h(k) \\ h^\dagger(k) & \epsilon \end{pmatrix} \quad (16)$$

where

$$h(k) = \begin{pmatrix} t_1 & t_2 & 0 & \cdots & t_2 e^{ik} \\ 0 & t_1 & t_2 & \ddots & 0 \\ \vdots & \ddots & \ddots & \ddots & \vdots \\ \vdots & \ddots & \ddots & t_1 & t_2 \\ 0 & \cdots & \cdots & 0 & t_1 \end{pmatrix} \quad (17)$$

and

$$\epsilon = \begin{pmatrix} V & 0 & \cdots \\ 0 & 0 & \ddots \\ \vdots & \ddots & \ddots \end{pmatrix}. \quad (18)$$

The chiral basis is defined as the basis in which the Hamiltonian takes the form of

$$\mathcal{H}_{\text{CPH}} = \chi^\dagger H \chi \quad (19)$$

where $\chi = (b_1, b_3, \dots, b_{2N-1}, b_2, b_4, \dots, b_{2N})^T$. The winding number can be calculated numerically using a method adapted from the scheme of Ref. [43] for numerical evaluation of the Chern number. For numerical evaluation the Brillouin zone is discretized $k \mapsto k_a$ where a is a discrete index with the k_a spaced by the interval $\Delta k = |k_{a+1} - k_a|$. The Zak phase can be calculated using this discretization as

$$e^{-i\gamma_n} = e^{-i \oint A_n(k) dk} \approx e^{-i \sum_a A_n(k_a) \Delta k} \approx \prod_a [\psi_n^\dagger(k_a) \psi_n(k_{a+1})] \quad (20)$$

where we have employed the unit normalization of the wavefunction and the discrete derivative. The phase is then obtained by taking the principal value of the logarithm,

$$\gamma_n = \frac{i}{\pi} \ln \left(\prod_a \psi_n^\dagger(k_a) \psi_n(k_{a+1}) \right). \quad (21)$$

The product is taken over the Brillouin zone, $k_a \in [0, 2\pi]$. We choose to index the unit-cell such that the dimer hosting the control potentials is located on the first dimer of the unit cell. In the topological phase, $t_2/t_1 > 1$, the zero energy bands have winding numbers

$$\gamma_{20} = -1, \quad \gamma_{21} = +1 \quad (22)$$

and in the trivial phase, $t_2/t_1 < 1$, have winding numbers

$$\gamma_{20} = 0, \quad \gamma_{21} = 0. \quad (23)$$

This calculation demonstrates that it is appropriate to identify the soliton states as being topological.

C. Signatures of soliton state in the on-site admittance spectrum

To elucidate the electronic response of the device hosting SSH state we consider admittance. According to the fluctuation-dissipation theorem [44], the admittance is related to the number-number spectral density function $\rho_{n_i, n_j}(\omega)$, with the included modification provided by the capacitive matrix. A signature of this state is visible in the finite-frequency spectrum probed locally by measuring the site-dependent AC admittance via small-signal

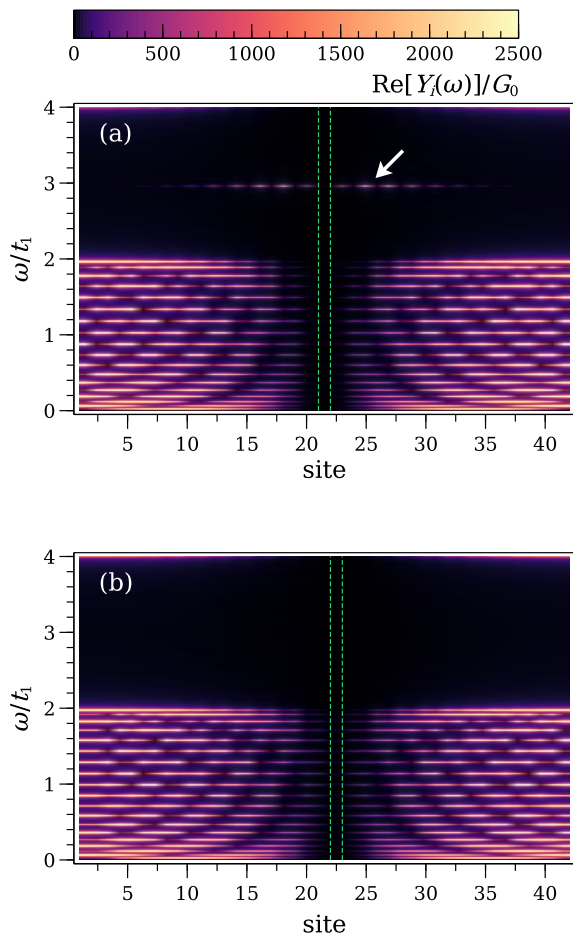


Figure 3. Real part of local admittance $\text{Re}[Y_i(\omega)]$ as a function of site i and frequency ω . (a) On-site potential applied on dimer 21-22 with a weak bond between the control sites. The white arrow indicates the peaks associated with transition to the soliton dimer states. (b) On-site potential applied on dimer 22-23 with a strong bond between the control sites. The ratio of the hopping elements is chosen to be $t_2/t_1 = 2.0$, and the applied control potential is $V/t_1 = 100.0$. We choose to work at temperature $T/t_1 = 0.005$ and the uniform potential shift is $V/t_1 = 2.992$ in both panels so that the average occupancy per site is $\langle n \rangle = 5.0$. The smearing factor in the Lorentzian representation of a delta function $\delta(x) \approx \eta/[\pi(x^2 + \eta^2)]$ is chosen to be $\eta = 0.005$. The scaling function chosen for scaling the color coding is $I(G) = 1 - e^{-\frac{G}{\delta G}}$, with $\delta G/G_0 = 25$, where $G_0 = 2e^2/h$.

analysis on the same gates where the polarizing gate potential is applied.

The exact expression is

$$\text{Re}[Y_i(\omega)] = \omega C_{g,i}^2 \sum_{k,l} \tilde{C}_{i,k}^{-1} \rho_{n_k, n_l}(\omega) \tilde{C}_{j,l}^{-1}. \quad (24)$$

Working in the approximation of a hopping Hamiltonian Eq. (6), $\rho_{n_i, n_j}(\omega)$ is given by the following expression involving the eigenvalues and wavefunctions

$$\rho_{n_k, n_l}(\omega) = \pi \sum_{\alpha, \beta} u_k^{(\alpha)} (u_l^{(\alpha)})^* u_l^{(\beta)} (u_k^{(\beta)})^* \times [n_B(\frac{\varepsilon_\beta}{T}) - n_B(\frac{\varepsilon_\alpha}{T})] \delta(\omega - \varepsilon_\alpha + \varepsilon_\beta). \quad (25)$$

Independently from the regime, the admittance is suppressed at the control dimer, due to the high detuning potential considered, Fig. 3. We note a quasi-continuum spectrum coming from the states above the gap. We note a discrete transition in Fig. 3(a) coming from the in-gap states, that is absent in the case that the system does not feature sub-gap states, Fig. 3(b). The admittance signal of the state oscillates in space, decaying eventually, being a measurement of the localization properties of the sub-gap state.

Alternatively, local spectroscopy of the the system using weakly-coupled metallic leads can reveal a similar information. We expect a peak in the conductance when the leads bias voltage align with the energy of the state. However, metallic probes can be detrimental for the shuttling protocol below, as they can induce uncontrolled changes between the two ground states.

D. Shuttling protocol the SSH soliton state

Now, we consider shuttling the soliton state by a single dimer via an adiabatic sweep of the potential controlling two neighboring islands. The coherence of the soliton state during the shuttling is dependent upon the protocol used for the potential sweep. The procedure which successfully maintains the state is illustrated in Fig. 4 and is referred to as protocol P1. For protocol P1, we initially consider large potentials on two adjacent sites belonging to the same cell. We focus on the topological regime ($t_2/t_1 > 1$), where the system shows in-gap states. The potential is slowly ramped down on these sites from a largely detuned situation to be on resonance. At the same time, we ramp up the potential of a neighboring cell. In order to break the degeneracy of the two soliton states (Fig. 2(c)), we choose a slightly different value ($\pm 10\%$) on the two control sites of the dimer, see Fig. 4(a). Figs. 4(c), (d), (e) depict the wavefunctions of several instantaneous eigenvalues around the mid-gap states during the shuttling protocol. The vertical dashed lines show the control dimer having strong on-site potential in Fig. 4(c), (e). We note a significant overlap of the time-evolved wavefunction with the final one, represented by the thin dashed line. We see that the mid-gap states always avoid crossing with the top of the valence band for a finite chain length, a necessary constraint for preserving the information encoded in them. They remain nearly degenerate until the on-site potential is about 4 times the bulk bandwidth, apart from the degeneracy point when the on-site potential is turned off in the middle of the protocol.

As a more quantitative measure of the protocol's success, in Fig. 5 we illustrate the overlap integral of the

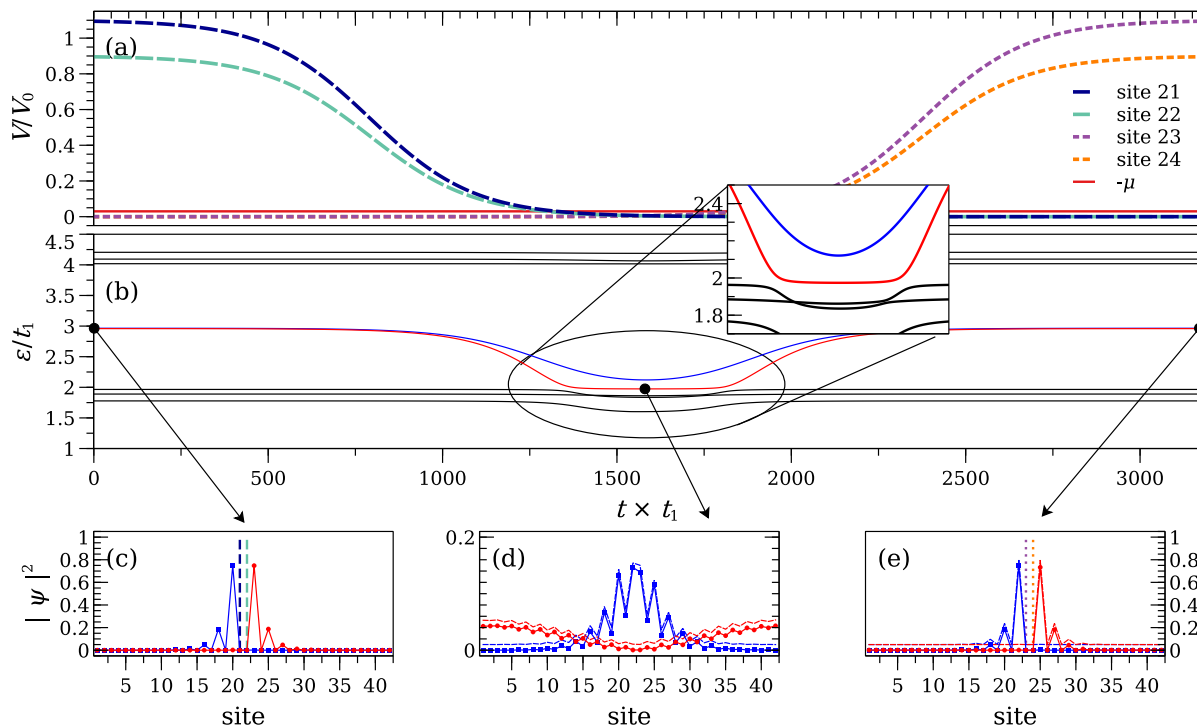


Figure 4. Adiabatic protocol P1 for shuttling the soliton dimer states from dimer 21-22 to dimer 23-24. (a) Profile of the ramp dimer potential in the course of the time steps. The degeneracy is broken by taking $1.1V_0$ on the left site and $0.9V_0$ on the right site of each dimer. Note that there is a uniform chemical potential applied to each site to keep the average number of particles fixed as in the previous figures. The time step $\Delta t = \pi/(1.1 \times 2 \times (|t_1| + |t_2|))$ is small enough so that the Nyquist frequency is higher than the bulk bandwidth. (b) The energies of the instantaneous eigenfunctions of the time-dependent Hamiltonian corresponding to the on-site potential from panel (a). Panels (c), (d), and (e): Snapshots of the time evolution of the single-particle wavefunction initialized in the corresponding initial eigenstate with the same color coding as in panel (b). The vertical dashed lines indicate the bond where the on-site potential is applied. The dashed curve on panel (e) is the instantaneous eigenstate at that time instant for visual comparison. The other parameters are identical as in Figs. 2, 3. In panels (d), (e), the dashed line wavefunctions are the instantaneous eigenfunctions shifted by a tiny amount for visibility.

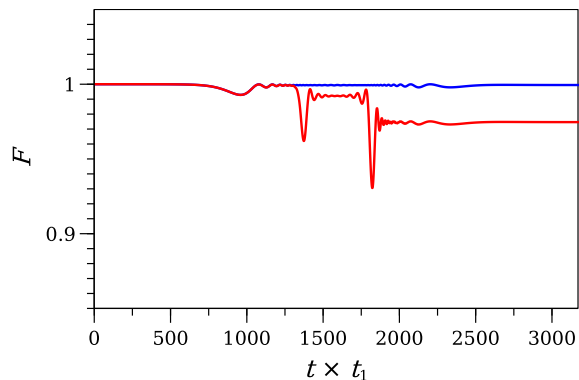


Figure 5. Fidelity for a shuttling process between neighboring dimers, Eq. (26) for the two mid-gap soliton states in Fig. 4 during protocol P1. Note the small range of values on the vertical axis.

time-evolved state $U(t) |u^{(\alpha)}(0)\rangle$ with the instantaneous eigenstate $|u^{(\beta)}(t)\rangle$

$$F_{\alpha}(t) = \left| \langle u^{(\alpha)}(t) | U(t) | u^{(\alpha)}(0) \rangle \right|^2, \quad \alpha \in \{s_1, s_2\} \quad (26)$$

for the two soliton states s_1, s_2 , which have color coding red and blue, respectively in Fig. 4.

We note the remarkably high fidelity level during this protocol that can be traced to the finite energy gap between the mid-gap states and the top of the valence band (Fig. 4(b)) throughout the whole procedure. The avoided crossing with the states at the quasi-continuum is smaller in the case of the lower-lying state (red). That results in a lower fidelity with respect to the higher state. In any case, it can be optimized to be arbitrarily close to $F = 1$ using slower sweep rates. We note the importance of breaking the degeneracy between the two sites of the dimer. In its absence, there is a significant conversion from one subgap state into the other, that can reach values up to 10% to 20%. This weight transference takes pace at the middle of the process, where the states hybridize with the continuum.

As an illustration of the importance of the relative time shift between the ramp-down and ramp-up phases in Fig. 4(a), we illustrate an alternative protocol P2 in Appendix A. In this case, we start the ramp-up well before the solitons hybridize with the continuum. Due to the orthogonality of the wavefunctions, the protocol fails

and $F \rightarrow 0$, Fig. 7.

IV. CONCLUSION

In this work, we have studied an array of coupled superconducting islands in the regime of strong charging energy. We studied the onset of topological states in this system when the Josephson energy has sublattice symmetry. This system shows mid-gap soliton states that are localized to a dimer with a weak link between the two sites using only electrostatic polarization. The topological nature of these soliton states is established quantitatively by demonstrating a non-zero winding number in the topological regime. We propose that signatures of these states are visible in the on-site AC admittance at frequencies corresponding to the energy difference from the bottom of the valence band to the mid-gap bound states. The site modulation of this spectrum coincides with that of the soliton wavefunctions. Finally, we discuss an adiabatic protocol for shuttling this bound state through a ring geometry.

ACKNOWLEDGMENTS

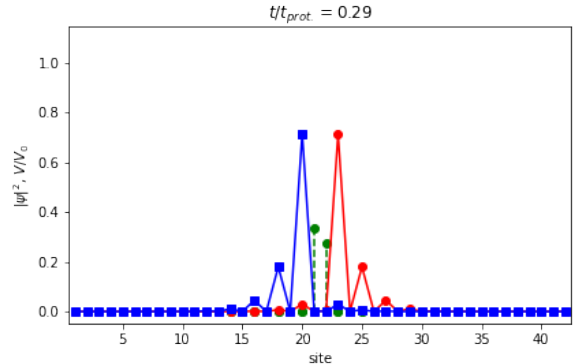
The authors wish to thank L. F. Banszerus, C. M. Marcus, and S. Vaitiekėnas for discussion of experimental feasibility. We further acknowledge L. Bascones, M. Burrello, O. Mansikkamäki, and E. Prada for helpful discussions. We acknowledge support from the Knut and Alice Wallenberg Foundation KAW 2019.0068, European Research Council under the European Union Seventh Framework ERS-2018-SYG 810451 HERO, Spanish CM “Talento Program” (project No. 2022-T1/IND-24070), and the University of Connecticut.

Appendix A: An illustration of a protocol P2

Figure 6 illustrates the protocol P2 that does not achieve an effective shuttling of the soliton dimer. The fidelity measure for P2, depicted in Fig. 7(b), clearly shows the inability of this protocol to shuttle the state to the neighboring control dimer. A crucial difference with protocol P1 is that the blue soliton state raises and gets pinned to the bottom of the conduction band as soon as the potential on dimer 23-24 is turned on. In effect, the fidelity of the blue state drops to less than half, because of the significant overlap with only the mid-gap red state. In the middle of protocol P2, the mid-gap state exchanges role with another completely orthogonal state, which evolves from the top of the valence band, with which the former mid-gap state has zero overlap. Thus, the fidelity of the red state abruptly drops to zero. When the potential on dimer 21-22 is turned off, the higher energy state drops from the conduction band in the middle of the gap. However, it has a negligible overlap with the

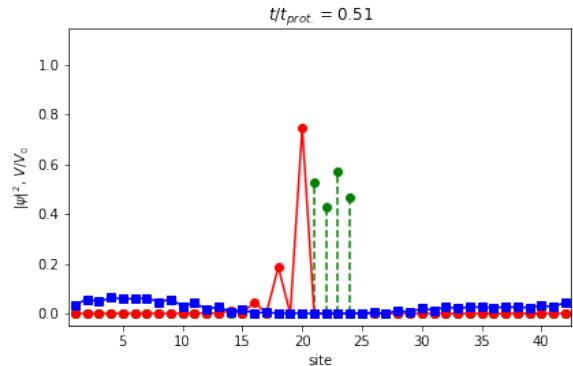
newly shifted mid-gap bound state, and the fidelity of the blue state has another significant drop.

Appendix B: Animations of shuttling protocols over the whole ring



Video 1. Animation showing the full time evolution of the soliton states according to protocol P1. Red (blue) curve are the wavefunctions initiated in the corresponding mid-gap soliton state in Fig. 4. The green dashed curved is the scaled value of the on-site control potential. The time t_{prot} is the time it takes for one dimer shift during protocol P1, $t_{\text{prot}} t_1 = 3.170 \times 10^3$.

The whole procedure over repeated over the ring is depicted in Video 1 for P1 and Video 2 for P2, respectively. We note the importance of a buffer phase of strong constant potential on the respective control dimer between the ramps, which is chosen to be of equal duration as the ramp up (down) phase. We depict the fidelity of



Video 2. Animation showing the full time evolution of the soliton states according to protocol P2. Because of the lack of a relative time shift between the ramp-down and ramp-up phases, the time it takes for one dimer shift during protocol P2 is shorter, $t_{\text{prot}} \times t_1 = 1.585 \times 10^3$.

both protocols across the whole ring in Fig. 8. As can be seen, the fidelity is preserved for both states to appreciable levels during the whole protocol P1, with the lower

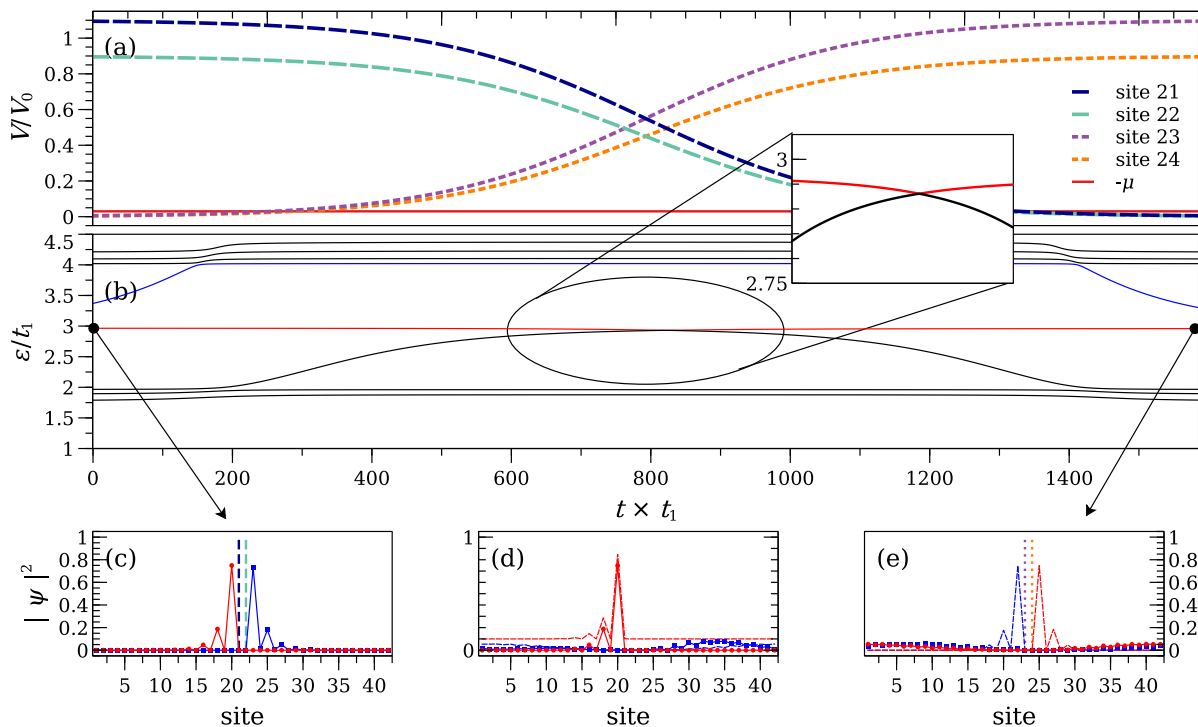


Figure 6. The protocol P2 that does not work analogously to Fig. 4, with the only difference in the relative time shift of the ramp-down and ramp-up .

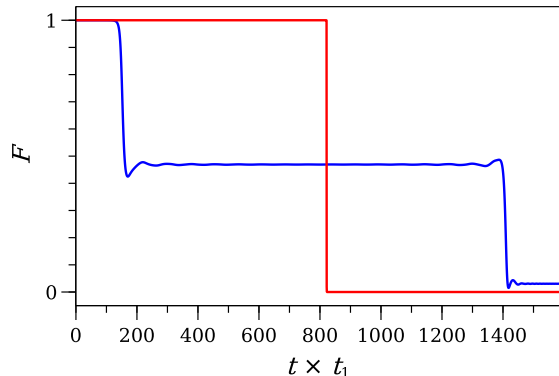


Figure 7. The fidelity characteristics as in Fig. 5 for the protocol depicted in Fig. 6.

energy red state having a marginally smaller value for the same reasons as in Fig. 5. For protocol P2, on the other hand, after an accidental reemergence of fidelity during the first two steps, there is a systematic, significant drop, illustrating again the inapplicability of this protocol for shuttling the soliton states.

[1] C. Neill, T. McCourt, X. Mi, Z. Jiang, M. Y. Niu, W. Mroczkiewicz, I. Aleiner, F. Arute, K. Arya, J. Atalaya, R. Babbush, J. C. Bardin, R. Barends, A. Bengtsson, A. Bourassa, M. Broughton, B. B. Buckley, D. A. Buell, B. Burkett, N. Bushnell, J. Campero, Z. Chen, B. Chiaro, R. Collins, W. Courtney, S. Demura, A. R. Derk, A. Dunsworth, D. Eppens, C. Erickson, E. Farhi, A. G. Fowler, B. Foxen, C. Gidney, M. Giustina, J. A. Gross, M. P. Harrigan, S. D. Harrington, J. Hilton, A. Ho, S. Hong, T. Huang, W. J. Huggins, S. V. Isakov, M. Jacob-Mitos, E. Jeffrey, C. Jones, D. Kafri, K. Kechedzhi, J. Kelly, S. Kim, P. V. Klimov, A. N. Ko-

rotkov, F. Kostritsa, D. Landhuis, P. Laptev, E. Lucero, O. Martin, J. R. McClean, M. McEwen, A. Megrant, K. C. Miao, M. Mohseni, J. Mutus, O. Naaman, M. Neeley, M. Newman, T. E. O'Brien, A. Opremcak, E. Ostby, B. Pató, A. Petukhov, C. Quintana, N. Redd, N. C. Rubin, D. Sank, K. J. Satzinger, V. Shvarts, D. Strain, M. Szalay, M. D. Trevithick, B. Villalonga, T. C. White, Z. Yao, P. Yeh, A. Zalcman, H. Neven, S. Boixo, L. B. Ioffe, P. Roushan, Y. Chen, and V. Smelyanskiy, Accurately computing the electronic properties of a quantum ring, *Nature* **594**, 508 (2021).

[2] I. M. Georgescu, S. Ashhab, and F. Nori, Quantum sim-

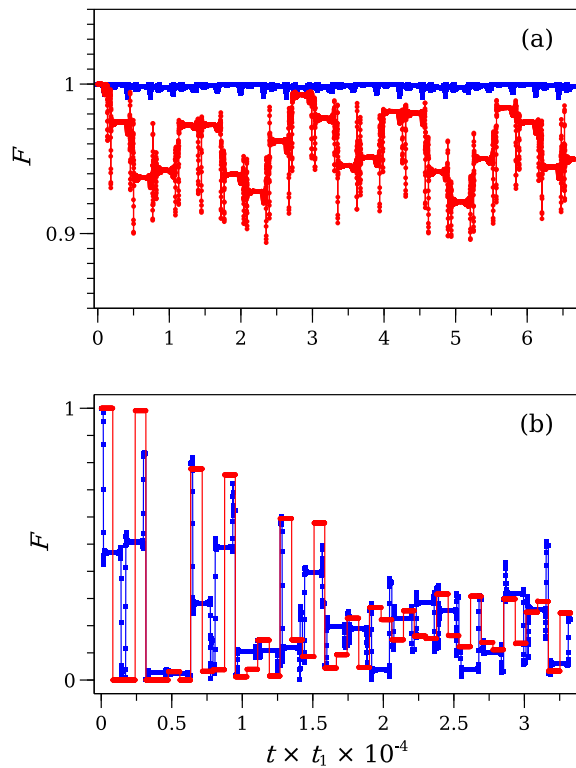


Figure 8. The fidelity characteristics as in Figs. 5, 7 for (a) protocol P1, (b) protocol P2. The color coding refers to the corresponding mid-gap states in Figs. 4, 6, respectively. Similar to Fig. 5, note the small range of values on the vertical axis in panel (a).

- ulation, *Reviews of Modern Physics* **86**, 153 (2014).
- [3] C. Monroe, W. C. Campbell, L.-M. Duan, Z.-X. Gong, A. V. Gorshkov, P. W. Hess, R. Islam, K. Kim, N. M. Linke, G. Pagano, P. Richerme, C. Senko, and N. Y. Yao, Programmable quantum simulations of spin systems with trapped ions, *Reviews of Modern Physics* **93**, 025001 (2021).
- [4] I. Bloch, J. Dalibard, and S. Nascimbène, Quantum simulations with ultracold quantum gases, *Nature Physics* **8**, 267 (2012).
- [5] S. Schmidt and J. Koch, Circuit QED lattices: Towards quantum simulation with superconducting circuits, *Annalen der Physik* **525**, 395 (2013).
- [6] L. J. Geerligs, M. Peters, L. E. M. de Groot, A. Verbruggen, and J. E. Mooij, Charging effects and quantum coherence in regular Josephson junction arrays, *Physical Review Letters* **63**, 326 (1989).
- [7] C. D. Chen, P. Delsing, D. B. Haviland, Y. Harada, and T. Claeson, Scaling behavior of the magnetic-field-tuned superconductor-insulator transition in two-dimensional Josephson-junction arrays, *Physical Review B* **51**, 15645(R) (1995).
- [8] H. S. J. van der Zant, W. J. Elion, L. J. Geerligs, and J. E. Mooij, Quantum phase transitions in two dimensions: Experiments in Josephson-junction arrays, *Physical Review B* **54**, 10081 (1996).
- [9] D. M. Basko, F. Pfeiffer, P. Adamus, M. Holzmann, and F. W. J. Hekking, Superconductor-insulator transition in Josephson junction chains by quantum Monte Carlo calculations, *Physical Review B* **101**, 024518 (2020).
- [10] C. G. L. Böttcher, F. Nichele, M. Kjaergaard, H. J. Suominen, J. Shabani, C. J. Palmström, and C. M. Marcus, Superconducting, insulating and anomalous metallic regimes in a gated two-dimensional semiconductor-superconductor array, *Nature Physics* **14**, 1138 (2018).
- [11] A. L. Rakhmanov, A. M. Zagoskin, S. Savel'ev, and F. Nori, Quantum metamaterials: Electromagnetic waves in a Josephson qubit line, *Physical Review B* **77**, 144507 (2008).
- [12] P. Macha, G. Oelsner, J.-M. Reiner, M. Marthaler, S. André, G. Schön, U. Hübner, H.-G. Meyer, E. Il'ichev, and A. V. Ustinov, Implementation of a quantum metamaterial using superconducting qubits, *Nature Communications* **5**, 5146 (2014).
- [13] J. D. Brehm, R. Gebauer, A. Stehli, A. N. Poddubny, O. Sander, H. Rotzinger, and A. V. Ustinov, Slowing down light in a qubit metamaterial, *Applied Physics Letters* **121**, 204001 (2022).
- [14] W. P. Su, J. R. Schrieffer, and A. J. Heeger, Solitons in Polyacetylene, *Physical Review Letters* **42**, 1698 (1979).
- [15] A. J. Heeger, S. Kivelson, J. R. Schrieffer, and W.-P. Su, Solitons in conducting polymers, *Reviews of Modern Physics* **60**, 781 (1988).
- [16] J. K. Asbóth, L. Oroszlány, and A. Pályi, *A Short Course on Topological Insulators*, 1st ed., Lecture Notes in Physics, Vol. 919 (Springer Cham, 2016).
- [17] H. Takayama, Y. R. Lin-Liu, and K. Maki, Continuum model for solitons in polyacetylene, *Physical Review B* **21**, 2388 (1980).
- [18] Y. Chen, X. Chen, X. Ren, M. Gong, and G.-c. Guo, Tight-binding model in optical waveguides: Design principle and transferability for simulation of complex photonics networks, *Physical Review A* **104**, 023501 (2021).
- [19] Y. Liu, X. Chen, and Y. Xu, Topological Phononics: From Fundamental Models to Real Materials, *Advanced Functional Materials* **30**, 1904784 (2020).
- [20] F. Mei, G. Chen, N. Goldman, L. Xiao, and S. Jia, Topological magnon insulator and quantized pumps from strongly-interacting bosons in optical superlattices, *New Journal of Physics* **21**, 095002 (2019).
- [21] Y.-H. Li and R. Cheng, Magnonic Su-Schrieffer-Heeger model in honeycomb ferromagnets, *Physical Review B* **103**, 014407 (2021).
- [22] P.-T. Wei, J.-Y. Ni, X.-M. Zheng, D.-Y. Liu, and L.-J. Zou, Topological magnons in one-dimensional ferromagnetic Su-Schrieffer-Heeger model with anisotropic interaction, *Journal of Physics: Condensed Matter* **34**, 495801 (2022).
- [23] E. J. Meier, F. A. An, and B. Gadway, Observation of the topological soliton state in the Su-Schrieffer-Heeger model, *Nature Communications* **7**, 13986 (2016).
- [24] S. de Léséleuc, V. Lienhard, P. Scholl, D. Barredo, S. Weber, N. Lang, H. P. Büchler, T. Lahaye, and A. Browaeys, Observation of a symmetry-protected topological phase of interacting bosons with Rydberg atoms, *Science* **365**, 775 (2019).
- [25] M. Atala, M. Aidelsburger, J. T. Barreiro, D. Abanin, T. Kitagawa, E. Demler, and I. Bloch, Direct measurement of the Zak phase in topological Bloch bands, *Nature Physics* **9**, 795 (2013).
- [26] M. Lohse, C. Schweizer, O. Zilberberg, M. Aidelsburger, and I. Bloch, A Thouless quantum pump with ultracold

- bosonic atoms in an optical superlattice, *Nature Physics* **12**, 350 (2016).
- [27] D. Xie, W. Gou, T. Xiao, B. Gadway, and B. Yan, Topological characterizations of an extended Su–Schrieffer–Heeger model, *npj Quantum Information* **5**, 55 (2019).
- [28] F. Mei, G. Chen, L. Tian, S.-L. Zhu, and S. Jia, Robust quantum state transfer via topological edge states in superconducting qubit chains, *Physical Review A* **98**, 012331 (2018).
- [29] W. Nie and Y.-x. Liu, Bandgap-assisted quantum control of topological edge states in a cavity, *Physical Review Research* **2**, 012076(R) (2020).
- [30] X. Guan and G. Chen, Interplay between topology and localization on superconducting circuits, arXiv preprint arXiv:2305.02486 [10.48550/arXiv.2305.02486](https://arxiv.org/abs/10.48550/arXiv.2305.02486) (2023).
- [31] A. Petrescu, H. E. Türeci, A. V. Ustinov, and I. M. Pop, Fluxon-based quantum simulation in circuit QED, *Physical Review B* **98**, 174505 (2018).
- [32] S. Parkin, X. Jiang, C. Kaiser, A. Panchula, K. Roche, and M. Samant, Magnetically engineered spintronic sensors and memory, *Proceedings of the IEEE* **91**, 661 (2003).
- [33] S. S. P. Parkin, M. Hayashi, and L. Thomas, Magnetic Domain-Wall Racetrack Memory, *Science* **320**, 190 (2008).
- [34] A. Fert, V. Cros, and J. a. Sampaio, Skyrmions on the track, *Nature Nanotechnology* **8**, 152 (2013).
- [35] S. Parkin and S.-H. Yang, Memory on the racetrack, *Nature Nanotechnology* **10**, 195 (2015).
- [36] U. Vool and M. Devoret, Introduction to quantum electromagnetic circuits, *International Journal of Circuit Theory and Applications* **45**, 897 (2017).
- [37] R. Fazio and H. van der Zant, Quantum phase transitions and vortex dynamics in superconducting networks, *Physics Reports* **355**, 235 (2001).
- [38] The mean-field contribution of the charging energy is an extra tight-binding element $\sum_{i,j} m_{i,j} b_i^\dagger b_j$, where $m_{i,j} = m_{j,i}^*$ is determined self-consistently
- $$m_{i,j} = \tilde{C}_{i,j}^{-1} \langle b_j^\dagger b_i \rangle.$$
- The assumption is that this matrix is a small correction to the hopping elements already included in Eq. (6).
- [39] J. Zak, Berry’s phase for energy bands in solids, *Physical Review Letters* **62**, 2747 (1989).
- [40] M. Eliashvili, D. Kereselidze, G. Tsitsishvili, and M. Tsitsishvili, Edge States of a Periodic Chain with Four-Band Energy Spectrum, *Journal of the Physical Society of Japan* **86**, 074712 (2017).
- [41] M. Maffei, A. Dauphin, F. Cardano, M. Lewenstein, and P. Massignan, Topological characterization of chiral models through their long time dynamics, *New Journal of Physics* **20**, 013023 (2018).
- [42] P. J. Wong, *Interactions and Topology in Quantum Matter: Auxiliary Field Approach & Generalized SSH Models*, Ph.D. thesis, University College Dublin (2022).
- [43] T. Fukui, Y. Hatsugai, and H. Suzuki, Chern Numbers in Discretized Brillouin Zone: Efficient Method of Computing (Spin) Hall Conductances, *Journal of the Physical Society of Japan* **74**, 1674 (2005).
- [44] R. Seoane Souto, D. Kuzmanovski, and A. V. Balatsky, Signatures of odd-frequency pairing in the Josephson junction current noise, *Physical Review Research* **2**, 043193 (2020).